Navigation Around Unknown Space Objects
Using Visible-Thermal Image Fusion

Eric J. Elias *

Massachusetts Institute of Technology, Cambridge, MA, 02139, USA

Michael Esswein †

The Charles Stark Draper Laboratory Inc., Cambridge, MA 02139, USA

Jonathan P. How ‡ and David W. Miller §

Massachusetts Institute of Technology, Cambridge, MA 02139, USA

As the popularity of on-orbit operations grows, so does the need for precise navigation around unknown resident space objects (RSOs) such as other spacecraft, orbital debris, and asteroids. The use of Simultaneous Localization and Mapping (SLAM) algorithms is often studied as a method to map out the surface of an RSO and find the inspector's relative pose using a lidar or conventional camera. However, conventional cameras struggle during eclipse or shadowed periods, and lidar, though robust to lighting conditions, tends to be heavier, bulkier, and more power-intensive. Thermal-infrared cameras can track the target RSO throughout difficult illumination conditions without these limitations. While useful, thermal-infrared imagery lacks the resolution and feature-richness of visible cameras. In this work, images of a target satellite in low Earth orbit are photo-realistically simulated in both visible and thermal-infrared bands. Pixel-level fusion methods are used to create visible/thermal-infrared composites that leverage the best aspects of each camera. Navigation errors from a monocular SLAM algorithm are compared between visible, thermal-infrared, and fused imagery in various lighting and trajectories. Fused imagery yields substantially improved navigation performance over visible-only and thermal-only methods.

I. Introduction

Oᴘᴇʀᴀᴛɪɴɢ in close proximity to resident space objects (RSOs)—such as asteroids, spacecraft, and orbital debris—is becoming increasingly common and essential. Close inspection and sample collection of asteroids may be required for scientific missions. Inspection of unknown spacecraft would support space situational awareness. Docking with the spacecraft may be needed for repair missions. Orbital debris may need to be intercepted and de-orbited. The spacecraft performing the inspection (the inspector) requires precise knowledge of its position and attitude relative to the RSO of interest (the target). This navigation solution is used for collision avoidance, predicting trajectories, planning maneuvers, characterizing the dynamics of the target, and creating a dense reconstruction of the target's shape and surface. This type of inspection scenario is illustrated in Fig. 1.

Target objects can be categorized into two classes: cooperative and uncooperative. Cooperative objects are designed to assist with the navigation of the inspector spacecraft in some way. As a result, they have navigation aids for inspectors to utilize, such as retroreflectors, and communicate their sensor measurements with the inspector.

This work focuses on uncooperative targets, which are not designed to interface with an inspector in any way. Uncooperative targets are considered "known" if a 3D model of the target's shape is available to the inspector prior to rendezvous. An inspector can estimate its position and attitude relative to the target (known as pose estimation) by matching 2D monocular images to the 3D model [1, 2] or by matching a 3D point cloud obtained from lidar to the 3D model [3–7]. Cassinis et al. provide a general survey of these spacecraft pose estimation techniques [8].

However, a target is not always "known" prior to the mission. These uncooperative and unknown targets are much more difficult to handle because a model of the target needs to be created while simultaneously being used to find the

---

*Draper Scholar, Department of Aeronautics and Astronautics, Massachusetts Institute of Technology, AIAA Member

†Senior Member of Technical Staff, The Charles Stark Draper Laboratory Inc.

‡Ford Professor of Engineering, Department of Aeronautics and Astronautics, Massachusetts Institute of Technology, AIAA Fellow

§Professor Post Tenure, Department of Aeronautics and Astronautics, Massachusetts Institute of Technology, AIAA Fellow
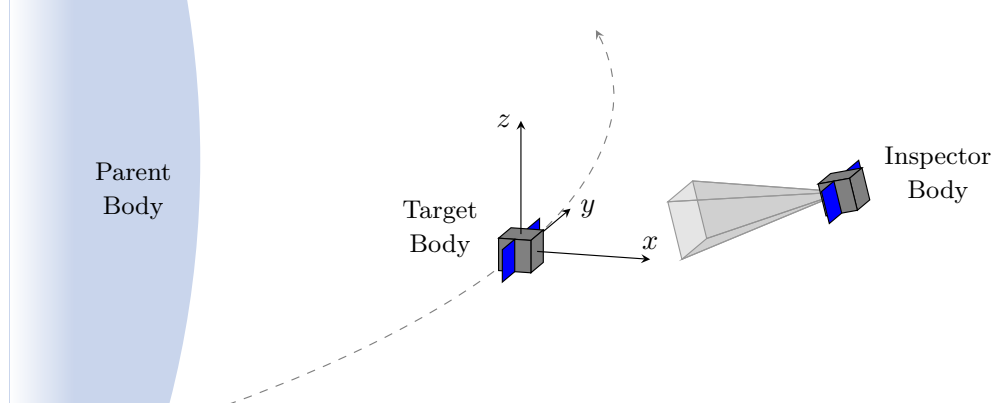
Fig. 1 A target and inspector orbiting around a parent body, with the inspector characterizing the target. The Hill coordinate frame is centered at the target, with the *x* axis pointing radially outwards, the *y* axis pointing in the target's direction of motion, and the *z* axis pointing in the direction of the target's orbital angular momentum vector.

relative pose of the inspector. This class of algorithms is known as Simultaneous Localization and Mapping (SLAM) and is a prominent focus of research in robotics [9]. Lichter et al. [10] first explored this problem in the context of space objects using collaborative 3D vision sensors (assumed to be uniformly distributed around the target), with a Kalman filter used to estimate the state, shape, and mass parameters of an unknown target. Sonnenburg et al. [11] used a set of stereo cameras to find the position of 3D features (high-contrast corners) on the target. These are inputs to an extended Kalman filter, which finds the relative pose of the inspector. A monocular camera can also be used to implement a similar system [12]. By tracking 2D features on the images of the target over multiple frames, the features can be triangulated and positioned in 3D space. This technique is known as structure from motion (SfM). Tweddle [13] implemented a SLAM algorithm assuming a stationary inspector that relies on a factor graph for mapping and pose estimation. A more in-depth description of this technique is found in Subsection II.D. Setterfield et al. [14] expanded on Tweddle's work so that it can handle a moving inspector. Orbital dynamics priors can also be incorporated into the SLAM estimate. Dor et al. [15] formulated a SLAM system to navigate around an unknown small asteroid in orbit around the Sun using these priors. The effects of the Sun's gravity, the asteroid's gravity, and solar radiation pressure are used to improve the estimated trajectory of the inspector and the map of the asteroid. One significant problem with these inspection missions is the large operating ranges between the inspector and target. Such ranges create degeneracies in SfM algorithms caused by weak-perspective projection, center-pointing trajectories, and dominant planar geometry of target satellites. These problems have been investigated by Florez et al. [16], who created a monocular pipeline robust to these degeneracies for spacecraft inspection.

Illumination conditions are often extremely problematic for the inspection of an RSO. Depending on the alignment of the inspector, the target, and the Sun, the target may be fully illuminated, partially illuminated, or completely in shadow from the viewpoint of the inspector. More likely is the case in which the inspector sees a target with dynamic shadows which constantly move over the target's surface. Additionally, in low Earth orbit (LEO) the target can have an orbital period as fast as 90 minutes, where it is common for the Sun to be completely eclipsed by Earth, as described in Subsection II.B. With dynamic shadows or full eclipse, a conventional camera is not able to track features on the target robustly.

Given these considerations, an additional sensor should be used by the inspector to improve navigation robustness. Lidar emits infrared lasers to measure the bearing and range of every point on the target. Unlike a camera, this active sensing method has the advantage of directly measuring the range to the target and is independent of illumination conditions. However, this also means that lidars use more power and are often significantly heavier and larger than a camera—constraints that are often difficult to accommodate in space vehicle design. Strong enough lidars also have the potential to damage fragile sensors on the target [17].

Thermal-infrared (TIR) cameras are robust to shadows and eclipses, while having a fraction of the footprint, weight, and power consumption compared to lidar. Instead of measuring visible light reflecting off of surfaces like visible (VIS) cameras do, TIR cameras detect thermal-infrared light being radiated or reflected from surfaces. They therefore measure the heat emitted by an object. For a given material, an object seen through a TIR camera is brighter when it is hot and

dimmer when it is cold. In LEO, a spacecraft is heated from many sources, including internal heating, from the Sun, and from Earth. More details about thermal dynamics are discussed in Subsection II.C. Even in eclipse conditions, a spacecraft's internal heating and Earth's thermal radiation still allow the spacecraft to be visible from an inspector's TIR camera. Compared to VIS cameras, the advantages of TIR are countered by their low resolution, noise, and low feature-richness. For example, a surface covered with VIS features may appear completely featureless in the TIR band.

Imagery from TIR cameras has been shown to be useful on flight demonstrations to the ISS [18, 19], as shown in Fig. 2. These missions demonstrate that using a TIR imager, the ISS is clearly visible over the entire orbit, even when fully eclipsed. The use of TIR has been studied for relative navigation around known and unknown RSOs, with a focus on how to utilize information from both VIS and TIR cameras simultaneously. Combining the information from VIS and TIR images creates a solution that has the advantages of each while hopefully avoiding their disadvantages. Civardi et al. [20] proposed a method to combine the VIS and TIR information to navigate around an unknown asteroid. SLAM is run separately for each sensor, and then the estimated relative pose from each SLAM solution is combined in an extended Kalman filter. While this method combines the estimation from the VIS and TIR sensors, it does so in a way that decouples the information between the two sensors. In other words, the features detected in the VIS image are not improving the navigation estimate obtained from the TIR image and vice versa. An approach that has been investigated for pose estimation around a known object [21–23] is the fusion of the VIS and TIR images at the pixel level before they are input into any navigation algorithm. This approach uses the joint information in both sensors to create a navigation estimate, rather than fusing two decoupled pose estimates.

(a) Range of 1.7 km while eclipsed from the Sun.

(b) Range of 300 m while illuminated by the Sun.
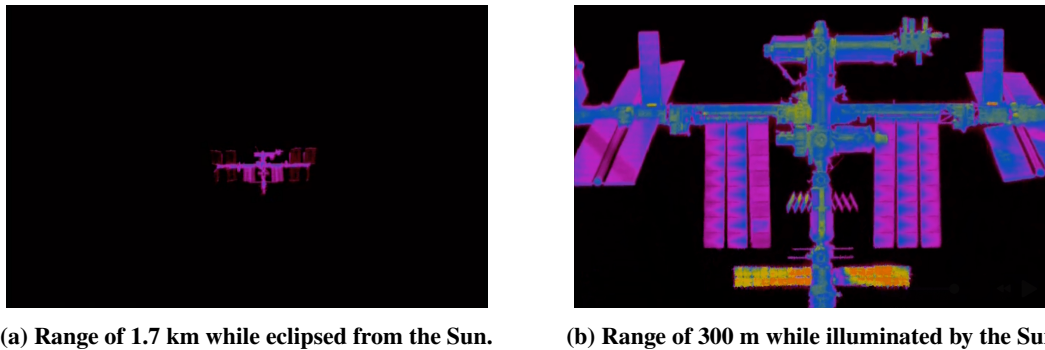
Fig. 2   The ISS as seen from the TIR imager of the TriDAR vision system during rendezvous operations on STS-131 [18].

This work investigates the use of VIS/TIR fused images compared to VIS-only or TIR-only images as inputs to a SLAM algorithm. This is the first time pixel-level VIS/TIR fusion is used for navigation around an unknown spacecraft in LEO, to the authors' best knowledge. Specifically, the main contributions are:

- A photo-realistic simulation of an inspector pointing its visible and thermal-infrared cameras at an unknown target spacecraft is created. Relative orbital dynamics, eclipse conditions, and other environmental conditions are incorporated in both the visible and thermal-infrared simulations.
- Renderings of many representative scenarios from an inspection mission are generated in both visible and thermal-infrared bands. Pixel-level fusion and image processing techniques are then applied to create visible-thermal composite images of the simulated spacecraft. Various trajectories, lighting conditions, and ranges are included in the dataset.
- Simulated inspection imagery is fed into a monocular SLAM algorithm that estimates the inspector's trajectory without any prior knowledge of the target's shape. An in-depth analysis is performed on the navigation errors and SLAM performance from each scenario and sensing modality. These tests focus on comparing the performance of visible-only, thermal-only, and visible-thermal fusion methods of navigation, demonstrating that fusion achieves superior performance.

The remainder of this paper is organized into five sections. Section II gives an overview of relevant background in relative orbital dynamics, eclipse conditions, thermal dynamics, SLAM, and VIS/TIR fusion. Section III discusses the details of the VIS and TIR simulator that is created. Section IV reviews the setup and integration of this simulated imagery with a SLAM algorithm. Section V compares the navigation performance of the SLAM algorithm between VIS-only, TIR-only, and VIS/TIR fused methods. Section VI concludes the paper and outlines directions of future work.

II. Background Overview

A. Relative Orbital Dynamics

Relative orbital dynamics are often viewed with a rotating reference frame, named the Hill frame, which is centered at the target body. This problem setup is shown in Fig. 1.

The relative motion of the inspector around the target can be linearized to create a set of coupled ordinary differential equations, named the Hill-Clohessy-Wiltshire (HCW) equations [24]

$$\ddot{x} - 2n\dot{y} - 3n^2x = 0 \tag{1a}$$

$$\ddot{y} + 2n\dot{x} = 0 \tag{1b}$$

$$\ddot{z} + n^2z = 0 \tag{1c}$$

where n is the mean motion of the target body. These equations fall under the assumptions that the target's orbit is nearly circular and unperturbed, and the range between the inspector and the target is small compared to the semi-major axis of the target's orbit.

When solving the HCW equations, constraints can be imposed that bound the relative orbit of the inspector around the target, such that these orbits take the form of closed ellipses that repeat over time in the Hill frame [25]. These solutions take the form of

$$x(t) = A_0 \cos(nt + \alpha) \tag{2a}$$

$$y(t) = -2A_0 \sin(nt + \alpha) + y_{\text{off}} \tag{2b}$$

$$z(t) = B_0 \cos(nt + \beta) \tag{2c}$$

where A_0, B_0, α, β, and y_{off} are integration constants to be satisfied by initial conditions. Similar bounded relative orbits have also been shown to exist for cases where the target has an elliptical orbit around the parent body, as well as where a non-spherical gravitational potential exists (such as LEO) [25].

The bounded relative orbits described above are useful for inspection missions, as they allow an inspector to remain close to the target while remaining in a thrust-free orbit around it. The simulations used in this work will have the inspector roughly follow these elliptical paths around the target.

B. Eclipse Conditions

A significant issue with visible cameras is their inability to see parts of the target that are not illuminated by the Sun. This occurs when the target is in between the inspector and the Sun, such that the target is backlit. However, a far more significant and common scenario is when Earth is eclipsing the target. To get a sense of how significant this effect is, we define the beta angle, β, as the angle between the solar vector and its projection onto the orbital plane [26]. This relationship is shown in Fig. 3.
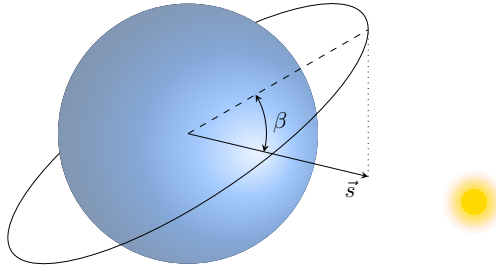
Fig. 3 β **is defined as the angle between the solar vector $\vec{s}$ and its projection onto the orbital plane.**

When β is small, the amount of time spent in eclipse is maximized. When β is at its maximum value of 90°, the orbital plane is normal to the solar vector, so the target is always exposed to the Sun. β varies over time as an orbit precesses due to non-spherical gravity, as well as by the solar vector changing as the Earth orbits the Sun. An example of how β affects the time spent in sunlight can be seen in Fig. 4. In LEO, it is common for objects to spend a significant amount of time in eclipse, sometimes exceeding 40% of the orbital period.
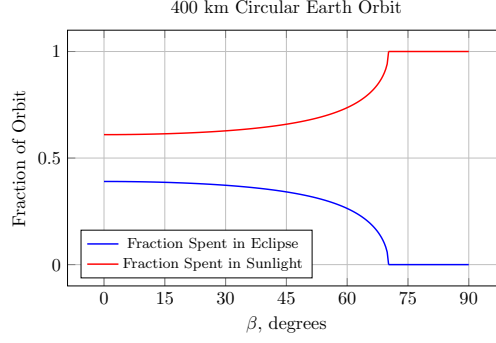
Fig. 4   The fraction of a 400 km circular Earth orbit spent in eclipse and sunlight, depending on β.

C. Thermal Dynamics

In order to simulate a spacecraft in the thermal band, it is important to first understand the sources of thermal radiation in LEO [26]. The sources we consider are internal heating, direct solar, Earth albedo, and Earth IR.

Internal Heating: A spacecraft has many sources of heat generated internally. This may consist of computers, communication systems, actuators, and heaters. The heat from these components conducts throughout the spacecraft and reaches the surface, where it is radiated away.

Direct Solar: The most significant source of spacecraft heating is by far direct sunlight. As long as the Sun is in view, it provides a source of radiation to the spacecraft with a constant intensity.

Earth Albedo: Sunlight reflects off Earth and back onto the spacecraft. This albedo is usually higher over land than ocean, and also has some dependence on latitude. For our simulation, we assume a constant IR albedo over Earth's surface.

Earth IR: Sunlight is absorbed by Earth and then radiated back into space as IR emission. Similar to Earth albedo, the intensity of this radiation is dependent on the location above Earth's surface. Again, we assume a constant Earth IR intensity over the surface.

D. Simultaneous Localization and Mapping

Simultaneous Localization and Mapping (SLAM) is the process of creating a map of an unknown environment while finding the position of an agent within that map. A detailed and modern report on the theory and methods can be found in the SLAM Handbook [9].

In this work, Kimera [27, 28] is used as the SLAM algorithm of choice. Kimera is a feature-based SLAM framework that distills priors, measurements, and dynamics into a factor graph to jointly optimize both the inspector's relative motion and the 3D positions of detected feature points on the target. In monocular mode, all Kimera requires is monocular camera images and IMU measurements. Two modules within Kimera are used: Kimera-VIO and Kimera-RPGO.

Kimera-VIO detects and tracks high-contrast points on the image (features) to estimate the motion of the inspector. This information is combined with the IMU measurements in a factor graph to estimate the states of the inspector and the 3D positions of each feature point (turning the 2D features on the image into 3D landmarks) over the entire smoothing window. Kimera uses a fixed-lag smoother in this case, meaning inspector states and landmark positions are repeatedly optimized within a recent time horizon. This visual-inertial odometry (VIO) effectively adds together many visual and inertial measurements, each consisting of small changes in relative pose of the inspector. As a result, the error in the state grows unbounded over time.

Kimera-RPGO bounds this error using loop closures. A loop closure occurs when the inspector re-visits the same view of the target. When a loop closure is detected, the relative pose between the current frame and the corresponding previous frame is found. Kimera-RPGO uses a separate factor graph from Kimera-VIO to set up the estimated full trajectory of the inspector. Every time a loop closure is detected, a new constraint is added to the factor graph and the full inspector trajectory is re-optimized.

Kimera's pipeline is summarized in the following list of steps:

Kimera-VIO: Creates a Visual-Inertial Odometry (VIO) estimate of the inspector's motion.
1) Detect new features in the current frame and match them to the detected features in the previous frame.

2) Perform geometric verification of feature matches.
3) Preintegrate IMU measurements between the last frame and the current frame.
4) Use visual and inertial measurements to jointly optimize for inspector states and landmark positions that fall within a recent time horizon (bundle adjustment).

Kimera-RPGO: Uses information from Kimera-VIO along with loop closure detections to create a Robust Pose Graph Optimization (RPGO) estimate.
1) At each frame, check for a loop closure. If no loop closure is detected, finish processing.
2) Find the relative pose between the current frame and the matching previous frame.
3) Add the loop closure constraint to the current trajectory estimate (which may already include previous loop closure constraints) and re-optimize the trajectory estimate.

E. VIS/TIR Fusion

Visible cameras are high resolution, can make out many features on a target, and are ubiquitous on spacecraft that are involved in proximity operations. However, they are unhelpful when a target is heavily shadowed. Thermal cameras are lower resolution and have difficulty making out many features that are seen in visible cameras, however they are able to see targets even in complete darkness. Combining these two modalities into a composite image yields a way to track features on a target regardless of the illumination conditions present.

Before image fusion, some pre-processing must take place. The input VIS and TIR images are often not the same resolution, with TIR usually a substantially lower resolution than VIS. However, the two images need to have matching resolution for the fusion methods to combine them. Civardi et al. [22] show that upscaling the TIR images to match the resolution of the VIS creates a fused image that is least sensitive to noise, as compared to downscaling the VIS images to match the TIR resolution. This approach is not only preferred because it is more robust to noise, but also because the higher resolution of the fused image allows for more precise placement of feature points, creating a more accurate navigation solution.

Civardi et al. also present an analysis of different image processing and fusion techniques to combine two separate VIS and TIR images into a fused image in the context of uncooperative spacecraft. Their analysis compares how closely the fused images retain the information from the input VIS and TIR images in the presence of noise, as well as the runtime of each algorithm. They find that two image fusion methods create the best resultant composites with a fast runtime: Anisotropic Diffusion-Based Fusion (ADF) [29] and Two-scale Image Fusion using Saliency Detection (TSIFSD) [30]. We compare the performance of TSIFSD and ADF in the context of SLAM around an unknown spacecraft.

TSIFSD and ADF both separate the input images into base layers, containing the lower frequency components of the image, and detail layers, containing the higher frequency components. The two algorithms differ in specifically how these layers are created and how they are fused.

1. Two-scale Image Fusion using Saliency Detection (TSIFSD) [30]

The input VIS and TIR images are first separated into their base layers and detail layers using a mean filter. The output of the mean filter creates the base layer, and the difference between the base layer and the input image is the detail layer. Next, visual saliency maps are created for each VIS and TIR image. These maps represent how "important" each pixel is in the context of its neighbors. These saliency maps are used to weight each pixel in the detail layers before they are combined with a weighted average into a fused detail layer. A simple average is taken between the VIS and TIR base layers to create a fused base layer. The fused detail and fused base layer are then added together, resulting in the final fused image.

2. Anisotropic Diffusion-Based Fusion (ADF) [29]

Anisotropic diffusion [31] is an iterative process that smooths an image at homogeneous regions, but preserves edges. This is used to separate the input VIS and TIR images into base layers and detail layers, similar to TSIFSD. The detail layers are then combined using a Karhunen–Loève transform [32–34], which decorrelates the information between the VIS and TIR layers into principal components. The strongest components are then combined to obtain the fused detail layer. After the base layers are combined with a simple average, the fused base and detail layers are added together.

III. Simulation Setup

A. Dynamics Propagation

MATLAB's high-fidelity numerical propagator is used to propagate the orbits of the inspector and the target, taking into account high-order gravity and atmospheric drag. For each simulated scenario, the orbital parameters of the inspector are adjusted to achieve the desired relative trajectory, closely following the HCW dynamics in Eq. 1.

B. Rendering

Blender is used as the rendering software of choice because of its photo-real rendering performance. The propagated dynamics of the target and inspector from MATLAB are imported into Blender. The inspector and a LEO environment are simulated to be as realistic as reasonably possible in both the VIS and TIR bands. This process starts with the creation of a target spacecraft, after which an environment is built around it. Since the simulation is in LEO, the environment includes Earth and the Sun. The VIS and TIR cameras also have unique properties that need to be included. These various steps in the rendering pipeline are illustrated in Fig. 6.
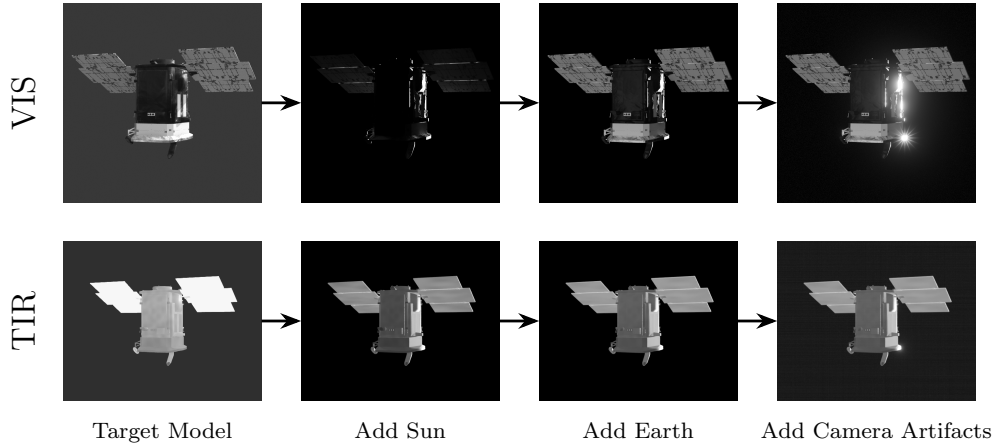
Fig. 5   The rendering framework, showing the effects of each simulation component.

1. Target Spacecraft

A 3D model of CloudSat from NASA's 3D model repository is imported into Blender as the target vehicle. This model includes the mesh of CloudSat, as well as the relevant colors, textures, and material properties. For the VIS renderings, the imported 3D model remains mostly unchanged. However, significant changes were made to a duplicated 3D model to simulate the appearance of the spacecraft in the TIR band.

To emulate internal heating of the spacecraft, a randomized emission texture is applied over the surface. This causes some parts of the spacecraft to be slightly brighter (warmer) and others to be slightly dimmer (cooler). The simulation of the surface heating due to external sources is achieved with a grey-colored texture, so when the thermal emission from the Sun and Earth is stronger, the surface is brighter and when they are weaker, the surface is dimmer. However, this ignores the conduction of heat towards the unlit sides of the spacecraft, as well as the storage of heat especially after orbital sunset. To solve this, the emission of each part of the spacecraft is separately hand-animated to reproduce the thermal conduction behavior seen on orbit. Larger and more thermally-massive components such as the spacecraft bus are animated to experience slow temperature changes, while low-mass components such as the solar array are animated with fast temperature changes, particularly during transitions between day and night.

2. Environment

In the VIS simulation, the two significant illumination sources are the Sun and Earth albedo. The Sun is simulated as an inertially fixed point source infinitely far away. The Earth is simulated photo-realistically as a sphere, with land, water, and cloud textures applied from satellite imagery. Atmospheric scattering is also included in this simulation. The rendering of Earth has a significant effect on the lighting of the target spacecraft, often filling in the harsh shadows left

by the Sun. This work does not plan to study the effects on tracking performance of Earth in the background of images, so the direct visibility of Earth is excluded from the renderings. However, it has been shown that the use of TIR imagery is far more robust to the clutter of Earth in the background [35].

The TIR simulation replaces Earth with a sphere that is grey. This color emulates the Earth albedo, such that the incident solar light is reflected. An emission property is also added, causing the Earth model to radiate light, emulating TIR radiation from Earth's surface and atmosphere. The Sun is modeled as an inertially fixed light source that is large in order to avoid any harsh shadowing on the target spacecraft in the TIR band. The simulation of Earth—including Earth albedo and Earth IR—is shown in Fig. 6.

(a) VIS   (b) TIR
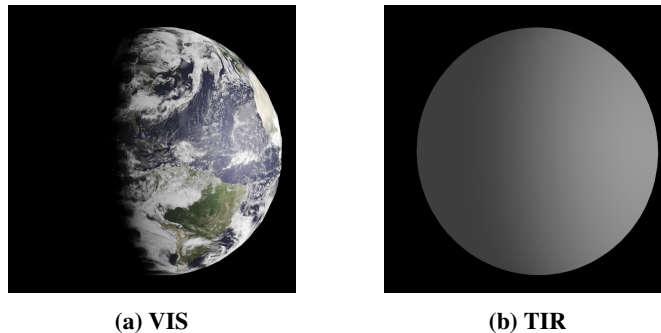
Fig. 6   Earth as simulated using Blender in the VIS and TIR bands.

3. Camera

For each type of imager, commonly used camera resolutions are chosen with full specifications laid out in Table 1. A separate camera field of view is used in the 50 m Range scenario. This ensures the target is large enough in the cameras' frames so that a reasonable number of features can be detected.

Table 1   VIS and TIR camera properties used in the simulations.

	VIS Camera	TIR Camera
Resolution, pixels	1024×1024	640×512
FoV	$25° \times 25°$	$31.25° \times 25°$
FoV (50 m Range)	$8° \times 8°$	$10° \times 8°$

Lens glare and bloom are added to the rendered images to replicate the artifacts seen through real cameras. These effects are often seen in the VIS camera due to reflections of the Sun off the target, which cause a large part of the image to be overexposed. The same glare and bloom effects are applied to the TIR images, however the limited strength of specular reflections causes these effects to be limited.

Another significant camera artifact is noise. A small amount of Gaussian noise is added to the VIS camera to simulate the electronic noise inherent to the camera. Most TIR cameras use an uncooled microbolometer imager which, unlike other types of TIR imagers, do not require a cryogenic cooler. However, the lack of cooling creates significant noise in the form of fixed-pattern noise (FPN) consisting of vertical and horizontal streaks across the image [36]. This FPN is added to the rendered TIR images, along with standard Gaussian noise.

C. Scenarios

Over all scenarios, the orbital parameters for the target remain the same. A semi-major axis of 6,778 km and an inclination of 51.6° are used, representing an altitude of approximately 400 km. No translational maneuvers are simulated in any case. The Sun is placed such that β is minimized, creating a worst-case scenario for eclipse conditions where approximately 40% of each scenario has the Sun eclipsed by Earth.

The attitude of the inspector is set such that the camera boresight is always pointed at the center of the target, and that the target's vertical axis is aligned vertically in the inspector's image frame.

Each scenario is propagated for three orbital periods. The period of each propagated orbit is 1.5 hours, so each scenario has a duration of 4.5 hours. Six scenarios are simulated, each representing unique trajectory, illumination, and attitude configurations. The details are as follows:

1. 15 m Range: The target satellite's attitude is inertially fixed. A relative trajectory that retains a nearly constant 15 m range between the target and inspector is used, which is retraced with each orbit.

2. 15 m Range, Fully Lit: The same as Scenario 1, however in the VIS rendering the target is perfectly illuminated from the inspector's position. This simulates a best-case scenario where there are no shadows and no eclipse in the high-resolution and feature-rich VIS images. The TIR renderings are exactly the same as in Scenario 1.

3. 15 m Range, Rotating Target: The same as Scenario 1, however the target is not inertially fixed and spins about its z-axis (parallel to z-axis in the ECI frame) at 5×10^{-4} rad/s in the opposite direction as the inspector's motion. This causes the target to have constantly moving shadows. While the relative trajectory is repeated for each orbit in the Hill frame, the target is rotating under the trajectory, causing the inspector to see a unique view of the target at almost all points in this scenario.

4. 15 – 25 m Range: The target satellite's attitude is inertially fixed. A relative trajectory with a range that oscillates between 15 m and 25 m over each orbit is used. This trajectory is retraced with each orbit.

5. 50 m Range: The target satellite's attitude is inertially fixed. A relative trajectory that retains a nearly constant 50 m range between the target and inspector is used, which is retraced with each orbit. A narrower set of cameras is used to retain good feature observability.

6. Flyby: The target satellite's attitude is inertially fixed. A relative trajectory is used that has a secular drift in the along-track direction. This creates a case where the range between the target and inspector is very dynamic, reaching a minimum of 12 m and a maximum of 38 m.

Out of these six scenarios, four unique relative inspector trajectories are used, as shown in Fig. 7. The inspector in Scenarios 1 and 3 follows the same trajectory in the Hill frame. However, Kimera assumes a static environment, so for Scenario 3, Kimera must perform estimation in the body frame of the target instead of the Hill frame. This trajectory becomes more complex in the fixed body frame of the target, as shown in Fig. 8.


(a) 15 m Range　　　**(b) 15 – 25 m Range**　　　**(c) 50 m Range**　　　**(d) Flyby**
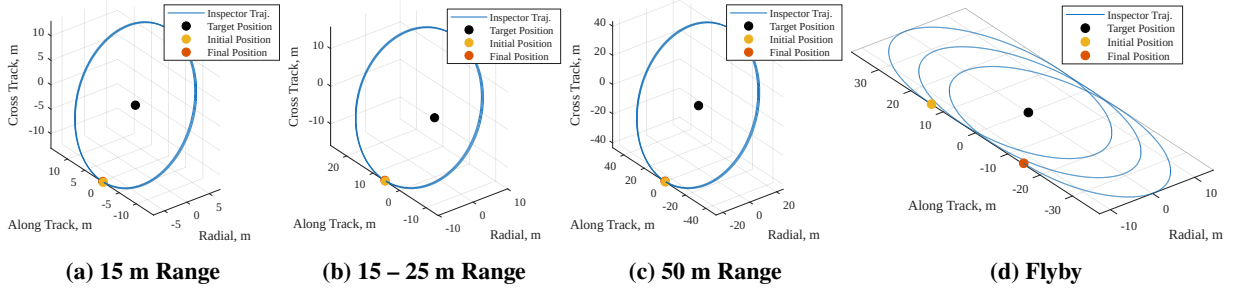
Fig. 7　Four unique relative trajectories are generated to create the scenarios. All trajectories are shown in the Hill frame over three orbits.

D. Relative Dynamics Measurements

Kimera requires translational acceleration and rotational velocity measurements relative to an inertially fixed environment. These measurements are combined with visual data to create the estimated state of the inspector. In most terrestrial SLAM use cases, these measurements are from accelerometers and gyroscopes mounted alongside the camera.

The dynamics of an on-orbit inspector behave very differently from the dynamics of a ground robot or UAV, however. Against Kimera's assumptions, the environment being mapped (the target RSO in this case) may not have an attitude that is inertially fixed if it has some rotational velocity. Similarly, the target's inertial position is certainly not fixed as it is orbiting Earth. As a result, the SLAM formulation needs to be adjusted to estimate the rotational velocity of the target and to incorporate the relative orbital dynamics between the target and inspector. Dor et al. formulate a SLAM framework that handles this complication of frames [15].
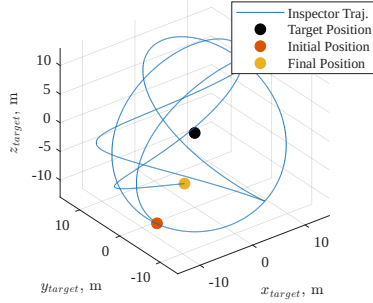
Fig. 8 The relative inspector trajectory for the 15 m Range, Rotating Target scenario in the body frame of the rotating target.

In order to simplify the problems arising from a non-inertially-fixed target to instead focus on the problem of visible-thermal fusion, this work assumes we have some noisy translational acceleration and rotational velocity measurements relative to the body frame of the target. Rotational velocity measurements are simulated using the ground truth relative trajectory with added noise, random walk, and bias instability to match measurement errors seen from a gyroscope. Relative acceleration measurements are also simulated using the ground truth relative trajectory. Relative orbital dynamics are the primary method to find these acceleration measurements [15]. As a result, errors are added to the simulated acceleration measurements to represent errors that would be found in the propagation of relative dynamics. Orbital propagation errors on the order of hundreds of meters over a propagation period of 24 hours are seen with common analytical propagation models [37]. The simulated relative acceleration measurements are therefore created with errors of this magnitude when integrated twice. MATLAB is used to generate the data using the parameters shown in Table 2.

Table 2 Error parameters used for the generation of simulated relative acceleration and relative angular velocity measurements.

	Relative Acceleration	Relative Angular Velocity
Noise Density	0	$1 \times 10^{-6} \, \text{rad/s}/\sqrt{\text{Hz}}$
Bias Instability	$1 \times 10^{-5} \, \text{m/s}^2$	$1 \times 10^{-6} \, \text{rad/s}$
Random Walk	0	$1 \times 10^{-6} \, \text{rad/s} \, \sqrt{\text{Hz}}$

IV. SLAM Setup
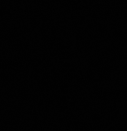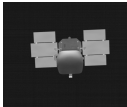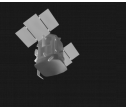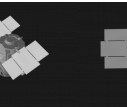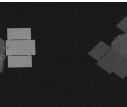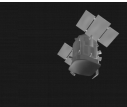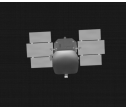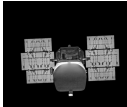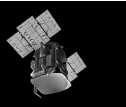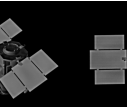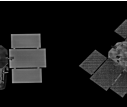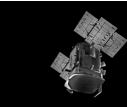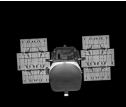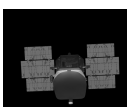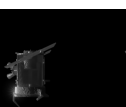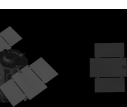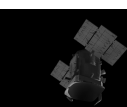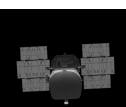
A. Image Processing

After images are generated in Blender, preprocessing is applied to increase contrast and reduce noise in the images before they are fed to Kimera. For each VIS and TIR frame, a threshold mask is used to separate the target from the dark background to minimize amplification of noise. Contrast Limited Adaptive Histogram Equalization (CLAHE) [38] is then applied to each VIS and TIR frame to improve local contrasts over the image and enhance the definition of edges, a common technique used to improve feature detection performance.

Before image fusion can be performed, the VIS and TIR images must be the same resolution and registered such that every pixel in the VIS image represents the same part of the target as the corresponding pixel in the TIR image. The TIR images are upscaled using bicubic interpolation and padding is added to match the VIS resolution. The TIR image is then registered to the VIS image using a transformation matrix that can be found prior during imager calibration.

After contrast enhancement, upscaling, and registration, the VIS and TIR images are fused. A visualization showing an example of the renders and fusion results is shown in Table 3.

Table 3   Simulated imagery of the CloudSat spacecraft at specified times on the inspector's trajectory for the various sensor types. This sequence shows the first orbit of the 15 m Range scenario. The full scenario has a similar sequence repeated twice more, for a total of three orbits.

B. Kimera Setup

For each scenario and each sensing modality, the corresponding monocular image sequences are input into Kimera. It should be noted that significant changes to Kimera's default parameters must be made for successful tracking and mapping, since Kimera is usually used for non-object-centric SLAM with wide field of view cameras. Parameters were changed for Kimera's feature tracker, optimizer, and loop closure detector modules. Additionally, some modifications had to be implemented in the software, such as handling of blank images (which the VIS camera sees during eclipse). All scenarios and sensing types use the same parameter set other than changes in camera intrinsics for the different camera resolutions and fields of view. Kimera's noise parameters are also set to match the noise in the relative dynamics measurements (as described in Subsection III.D).

The estimated trajectory output by Kimera is relative to the target body frame, so in the absence of a relevant prior, an infinite number of valid solutions exist in which both the target's landmark positions and the inspector's trajectory can be translated and rotated in any way. As a result, an initial estimate of the inspector's relative pose is input to anchor its trajectory estimate and the position of the target in Kimera's coordinate system. In reality, this initial relative pose can be arbitrarily chosen.

The estimated trajectory can be created in two ways. The first method evaluates the estimated pose as each measurement and image comes in over the course of the scenario. The second method uses the batch optimized estimate solved at the end of the trajectory, assuming all measurements and images are available from the full scenario. We follow the first method when analyzing the performance of this system. The real-time navigation errors are necessary to analyze due to their use in the closed-loop guidance and control of the inspector. While the batch method is useful for post-inspection analysis, this work focuses on navigation during an active inspection.

The camera images are input at 0.1 Hz and the relative dynamics measurements are input at 10 Hz. An example of Kimera's operation is seen in Fig. 9 and a full system architecture is included in Fig. 10.
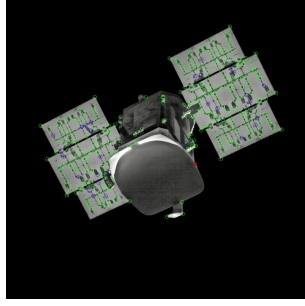
(a) Features are tracked on a TIR image of the target spacecraft. Green points are features that are detected in the current frame and are being tracked since previous frames. Blue points are features that have been detected, but are not yet tracked. Red points are outlier features.
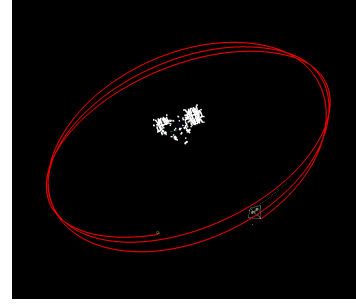
(b) The estimated 3D positions of the landmarks tracked on the target (white points) and the estimated trajectory of the inspector (red curve).

Fig. 9   Kimera tracks features on sequential images of the target spacecraft. The feature tracks are used to create a 3D map of the target and estimate the trajectory of the inspector.
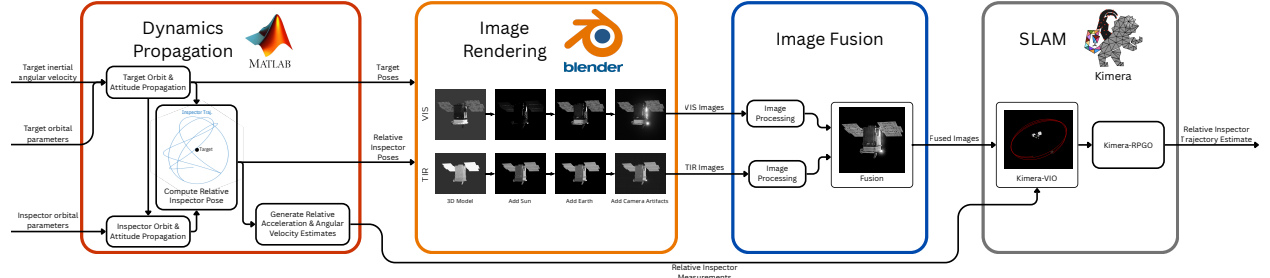
Fig. 10   The full pipeline used for dynamics propagation, rendering, fusion, and SLAM.

V. Results

The simulated relative position and attitude between the inspector and the target spacecraft is estimated using Kimera, using only monocular images and noisy relative measurements. The performance of the navigation solutions are compared between the various sensing modalities and scenarios.

An example of the error seen over the course of a run is shown in Fig. 11. For all runs, loop closures are never detected during the first circumnavigation around the target because each frame shows a new part of the target the inspector is viewing. Over this period, the pose error steadily grows as the visual-odometry measurements are integrated. The maximum errors are often seen at the end of the first circumnavigation. When the first loop closure is detected (usually at the beginning of the second circumnavigation), the pose error significantly decreases because the start of the second circumnavigation can be directly related to the start of the first circumnavigation, where the position and velocity have low error. Throughout the second and third circumnavigation, loop closures can be detected as the target revisits perspectives of the target. Although some loop closures may be of poor quality causing the errors to increase, most cause a drop in error and ultimately keep the errors bounded.

For each run, the position and rotation errors between the estimated and ground truth relative trajectories are found using evo [39], which averages them over the whole trajectory. These results are shown in Table 4. The maximum errors over each trajectory are also calculated and included in Table 5. Table 6 shows the number of loop closures detected out of the 1,661 frames in each run. The percent of frames during which successful tracking and mapping is achieved is shown in Table 7. The average number of inlier feature matches per frame is presented in Table 8, only including frames which had successful tracking and mapping.
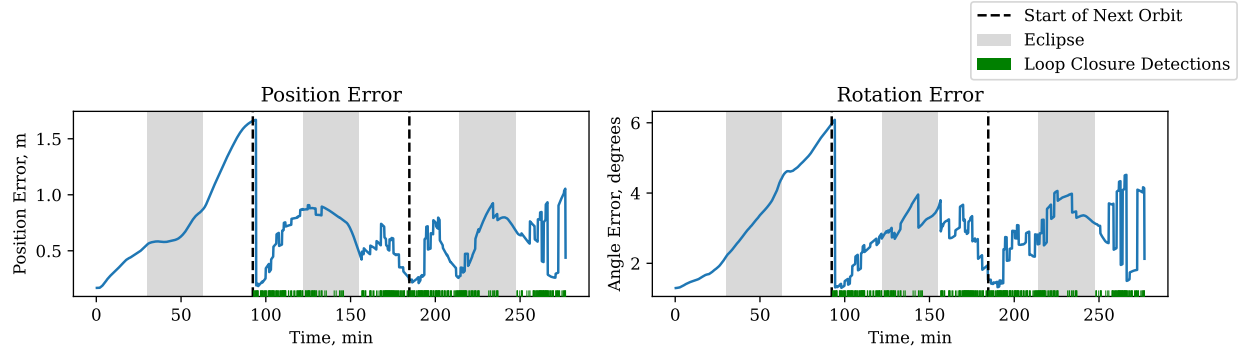
Fig. 11   The position and rotation error for the inspector over the 15 m Range scenario using TSIFSD fusion. In this case, the target is inertially fixed so each orbit around Earth is coincident with each circumnavigation of the inspector around the target. Loop closure detections are factored into the pose estimate every 5 detections to speed up runtime.

A. VIS

For the VIS camera, a wide range of errors is produced, heavily dependent on the scenario. Small errors are particularly noticeable in the fully lit scenario, where the VIS camera can see many high-quality features over the entire trajectory, as well as loop closures that can be detected during the eclipse period. Compared to the fixed target attitude case, the rotating target scenario has larger errors due to a complete lack of loop closure detections. The 15 – 25 m Range case has larger errors than the 15 m Range case because the target takes up a smaller area of the frame, decreasing the number of resolved features on the target. This is also accompanied by a weaker perspective, where the larger ranges cause increased depth uncertainty. In all these cases (except for the fully lit), the VIS camera is only able to successfully track for 60 – 65% of the frames. The remaining frames have the spacecraft in complete darkness because of the eclipse period.

The 50 m Range and Flyby scenarios experience unrecoverable failures in tracking and mapping. This is due to two contributing factors. First, the larger ranges seen in these cases cause very weak perspective. Especially in the 50 m Range scenario, this lack of parallax at the longer range causes extreme uncertainty in the estimated depth to each detected feature on the spacecraft. The second contributor is the eclipse conditions, during which navigation relies solely on the integration of orbital priors, resulting in a large rise in navigation uncertainty. Both these contributors of uncertainty ultimately result in a complete loss of tracking/mapping.

B. TIR

The navigation performance of using only the TIR camera is overall worse than the use of only the VIS camera. Errors in the 15 m Range scenarios and the 15 – 25 m Range scenario are all higher as compared to VIS. This is due to the lower resolution of the TIR camera, the lower number of features, and the noisier image quality. This also causes there to be far fewer loop closure detections. However, unlike the VIS camera, the TIR camera has a practically perfect tracking success over all frames in these scenarios, despite the periods of eclipse.

In the longer-range 50 m Range and Flyby scenarios, the TIR camera struggles like the VIS camera. The failures in these cases are caused by weak perspective and a low feature count.

C. Fused VIS/TIR

The performance of the TSIFSD and ADF fusion methods is superior to VIS-only and TIR-only performance in almost all metrics. These methods retain the high feature-richness and resolution of the VIS camera, while also adding the illumination-robust abilities of the TIR camera. The average and maximum errors seen with the fused methods are lower in almost every scenario. The number of loop closure detections is maximized because of the ability to detect them during eclipse using the TIR camera, as well as the use of high quality features from the VIS camera when able. These features allow Kimera to track both VIS and TIR features in the same frame, maximizing the number of features seen throughout every part of the image. Almost perfect tracking success is seen in all cases with the fused methods. TSIFSD has the best feature matching performance, while ADF loses some image detail in the fusion process and often

has fewer feature detections than the VIS camera.

The longer-range scenarios using fusion no longer experience unrecoverable failures as seen with the VIS and TIR cameras. While weak perspective is still a significant problem, the high resolution, feature-richness, and lack of eclipse are able to counter the degenerate effects of the large operating ranges.

The results also indicate that TSIFSD generally performs better than ADF. TSIFSD retains more detail in the fused images, shown by the significantly higher number of feature matches per frame. Accompanied by the fact that TSIFSD has a runtime almost an order of magnitude less than ADF [30], TSIFSD is the recommended method of fusion in this analysis.

Table 4   Average position and rotation errors over each run. Errors are between Kimera's estimate of the inspector's relative pose and the ground truth relative pose.

| | Position Error, meters | | | | Rotation Error, degrees | | | |
Scenario	VIS	TIR	Fused (TSIFSD)	Fused (ADF)	VIS	TIR	Fused (TSIFSD)	Fused (ADF)
15 m Range	0.92	1.51	<u>0.67</u>	**0.58**	3.08	5.43	<u>3.00</u>	**2.76**
15 m Range, Fully Lit	<u>0.48</u>	1.51	0.92	**0.35**	<u>2.08</u>	5.43	2.25	**1.70**
15 m Range, Rotating Target	1.88	2.99	**0.95**	<u>1.37</u>	<u>5.25</u>	13.74	**4.79**	6.56
15 – 25 m Range	3.60	3.40	**2.25**	<u>2.32</u>	6.83	11.33	<u>6.39</u>	**6.03**
50 m Range	69.26	7.46	<u>2.83</u>	**2.39**	17.50	7.44	<u>3.39</u>	**3.10**
Flyby	14.05	68.10	<u>3.18</u>	**2.63**	13.50	58.46	**4.70**	<u>6.49</u>
Average	15.03	14.16	<u>1.80</u>	**1.61**	8.04	16.97	**4.09**	<u>4.44</u>

Values in red denote cases with an unrecoverable failure in tracking and/or mapping.
Bold errors are the lowest for each sensing modality.
<u>Underlined</u> errors are the second lowest for each sensing modality.

Table 5   Maximum position and rotation errors over each run. Errors are between Kimera's estimate of the inspector's relative pose and the ground truth relative pose.

| | Position Error, meters | | | | Rotation Error, degrees | | | |
Scenario	VIS	TIR	Fused (TSIFSD)	Fused (ADF)	VIS	TIR	Fused (TSIFSD)	Fused (ADF)
15 m Range	3.89	4.92	**1.67**	<u>1.84</u>	9.26	19.21	**6.04**	<u>6.73</u>
15 m Range, Fully Lit	<u>1.24</u>	4.92	1.71	**0.91**	4.72	19.21	<u>4.66</u>	**4.38**
15 m Range, Rotating Target	3.73	7.41	**1.92**	<u>2.54</u>	<u>11.47</u>	27.57	**8.28**	12.06
15 – 25 m Range	**6.73**	11.53	<u>7.36</u>	7.87	**15.54**	28.37	<u>16.62</u>	20.74
50 m Range	350.94	19.42	<u>6.51</u>	**6.26**	62.28	14.62	<u>8.74</u>	**7.47**
Flyby	37.55	182.20	**6.53**	<u>7.58</u>	36.28	122.80	**11.20**	<u>12.64</u>
Average	67.35	38.40	**4.28**	<u>4.50</u>	23.26	38.63	**9.26**	<u>10.67</u>

Values in red denote cases with an unrecoverable failure in tracking and/or mapping.
Bold errors are the lowest for each sensing modality.
<u>Underlined</u> errors are the second lowest for each sensing modality.

Table 6 Number of loop closure detections in each run. Each loop closure represents an instance when an earlier view of the target spacecraft is revisited.

Scenario	VIS	TIR	Fused (TSIFSD)	Fused (ADF)
15 m Range	287	93	**437**	<u>383</u>
15 m Range, Fully Lit	624	93	<u>710</u>	**720**
15 m Range, Rotating Target	<u>0</u>	<u>0</u>	**4**	0
15 – 25 m Range	122	25	<u>202</u>	**217**
50 m Range	96	29	**375**	<u>359</u>
Flyby	0	0	<u>75</u>	**97**
Average	188	40	**301**	<u>296</u>

Values in red denote cases with an unrecoverable failure in tracking and/or mapping.
Bold counts are the largest for each sensing modality.
<u>Underlined</u> counts are the second highest for each sensing modality.

Table 7 Tracking/mapping success rate over each run. The success rate is calculated by counting the number of frames in which valid features are detected and mapped as landmarks, divided by the total number of frames.

Scenario	VIS	TIR	Fused (TSIFSD)	Fused (ADF)
15 m Range	<u>64.0%</u>	**100.0%**	**100.0%**	**100.0%**
15 m Range, Fully Lit	**100.0%**	**100.0%**	**100.0%**	**100.0%**
15 m Range, Rotating Target	64.1%	**99.9%**	98.7%	<u>99.3%</u>
15 – 25 m Range	61.3%	<u>99.9%</u>	**100.0%**	<u>99.9%</u>
50 m Range	32.0%	<u>81.6%</u>	**100.0%**	**100.0%**
Flyby	36.1%	46.0%	**96.6%**	<u>96.4%</u>
Average	59.6%	87.9%	<u>99.2%</u>	**99.3%**

Values in red denote cases with an unrecoverable failure in tracking and/or mapping.
Bold rates are the highest for each sensing modality.
<u>Underlined</u> rates are the second highest for each sensing modality.

Table 8 Average inlier feature matches per frame over each run, only including frames during which features are successfully tracked and mapped.

Scenario	VIS	TIR	Fused (TSIFSD)	Fused (ADF)
15 m Range	**123**	31	<u>122</u>	92
15 m Range, Fully Lit	96	31	**126**	<u>102</u>
15 m Range, Rotating Target	<u>96</u>	32	**108**	83
15 – 25 m Range	<u>84</u>	26	**91**	70
50 m Range	**127**	30	<u>123</u>	94
Flyby	<u>48</u>	34	**59**	47
Average	<u>96</u>	31	**105**	81

Values in red denote cases with an unrecoverable failure in tracking and/or mapping.
Bold counts are the highest for each sensing modality.
<u>Underlined</u> counts are the second highest for each sensing modality.

VI. Conclusion

This work presents a method to perform relative navigation of an inspector around an uncooperative and unknown target RSO in LEO using image-level fusion of visible and thermal-infrared imagery. The proposed approach takes advantage of the high resolution, high contrast, feature-richness, and low noise of the visible camera, while also incorporating the illumination robustness of the thermal-infrared camera. Unlike other methods that keep the visible and thermal-infrared separate until a final fusion step, this work combines the two sensing modalities as the first stage in the navigation pipeline, ensuring their information is jointly used during feature tracking and pose estimation.

A high-fidelity simulation of a target spacecraft is first created in both visible and thermal-infrared using Blender, incorporating the effects of internal heating, solar heating, Earth albedo, and Earth IR. This simulator is used to create six representative scenarios of an inspection mission, each with unique relative trajectories and lighting conditions. These images are fused into composite images using one of two methods: TSIFSD and ADF. The fused images are then input into a SLAM algorithm along with noisy relative acceleration and angular velocity measurements representing orbital dynamics priors. Compared to visible or thermal-infrared alone, the navigation solution using fused imagery estimates a far more accurate relative inspector trajectory. TSIFSD—which is the recommended fusion method from our analysis—decreases the position error by an average of 88% in the simulated scenarios over visible-only navigation, and by 87% over thermal-only navigation. Attitude error is improved by 49% and 76% compared to visible-only and thermal-only navigation, respectively. The fusion methods are especially advantageous in cases where the target RSO is in darkness due to the Earth eclipsing the Sun. Additionally, the large operating ranges between the inspector and target cause degenerate conditions for SLAM algorithms, which the fusion methods can overcome.

While this work shows the practicality of visible-thermal image fusion, some assumptions are made here that should be replaced before the use of this algorithm in flight. Namely, the generation of relative translational acceleration and rotational velocity measurements should realistically be replaced with a system that creates real-time estimates of the inspector's relative motion using orbital dynamics. A formulation created by Dor et al. [15] can be used to remove the assumptions used here.

The navigation methods presented here rely on image-level fusion between visible and thermal-infrared. However, another method of fusion could combine the visible and thermal information in the back-end optimization of the SLAM algorithm. Features can be tracked on visible and thermal images separately, followed by the 3D mapping of each landmark in a joint visible-thermal map of the target. In this framework, the stereo baselines between the visible and thermal cameras can be used to calculate the depth of features that are common between the two cameras. This navigation framework has already been tested for terrestrial navigation [40] and may offer an even better visible-thermal fusion method in the context of on-orbit inspection.

Although other sensor types such as lidar are also able to perform this type of relative navigation—and may even offer better performance—the use of visible and thermal-infrared cameras avoids the large size, weight, and power usage of lidars as any active mode of sensing is avoided. This approach allows for a small, lightweight, and low-power method of navigation around unknown RSOs while remaining robust to the harsh lighting conditions present in LEO. This opens up many new mission opportunities, such as the use of small, low-cost CubeSat spacecraft to perform complex proximity operation tasks.

References

[1] Sharma, S., and D'Amico, S., "Comparative assessment of techniques for initial pose estimation using monocular vision," *Acta Astronautica*, Vol. 123, 2016, pp. 435–445. Special Section: Selected Papers from the International Workshop on Satellite Constellations and Formation Flying 2015.

[2] Pauly, L., Rharbaoui, W., Shneider, C., Rathinam, A., Gaudillière, V., and Aouada, D., "A survey on deep learning-based monocular spacecraft pose estimation: Current state, limitations and prospects," *Acta Astronautica*, Vol. 212, 2023, pp. 339–360.

[3] Ruel, S., Luu, T., Anctil, M., and Gagnon, S., "Target Localization from 3D data for On-Orbit Autonomous Rendezvous & Docking," *2008 IEEE Aerospace Conference*, 2008.

[4] Opromolla, R., Rufino, G., Fasano, G., and Grassi, M., "LIDAR-based autonomous pose determination for a large space debris," *Proceedings of the International Astronautical Congress, IAC*, Vol. 2, 2014, pp. 1512–1520.

[5] Liu, L., Zhao, G., and Bo, Y., "Point cloud based relative pose estimation of a satellite in close range," *Sensors*, Vol. 16, No. 6, 2016, p. 824.

[6] Woods, J. O., and Christian, J. A., "Lidar-based relative navigation with respect to non-cooperative objects," *Acta Astronautica*, Vol. 126, 2016, pp. 298–311. Space Flight Safety.

[7] Perfetto, D. M., Opromolla, R., Grassi, M., and Schmitt, C., "LIDAR-based model reconstruction for spacecraft pose determination," *2019 IEEE 5th International Workshop on Metrology for AeroSpace (MetroAeroSpace)*, 2019.

[8] Pasqualetto Cassinis, L., Fonod, R., and Gill, E., "Review of the robustness and applicability of monocular pose estimation systems for relative navigation with an uncooperative spacecraft," *Progress in Aerospace Sciences*, Vol. 110, 2019, p. 100548.

[9] Carlone, L., Kim, A., Dellaert, F., Barfoot, T., and Cremers, D. (eds.), *SLAM Handbook: From Localization and Mapping to Spatial Intelligence*, Cambridge University Press, 2025.

[10] Lichter, M., and Dubowsky, S., "State, shape, and parameter estimation of space objects from range images," *IEEE International Conference on Robotics and Automation, 2004. Proceedings. ICRA '04. 2004*, Vol. 3, 2004, pp. 2974–2979 Vol.3.

[11] Sonnenburg, A., Tkocz, M., and Janschek, K., "EKF-SLAM based Approach for Spacecraft Rendezvous Navigation with Unknown Target Spacecraft," *IFAC Proceedings Volumes*, Vol. 43, No. 15, 2010, pp. 339–344. 18th IFAC Symposium on Automatic Control in Aerospace.

[12] Augenstein, S., and Rock, S. M., "Improved frame-to-frame pose tracking during vision-only SLAM/SFM with a tumbling target," *2011 IEEE International Conference on Robotics and Automation*, 2011, pp. 3131–3138.

[13] Tweddle, B. E., "Computer vision-based localization and mapping of an unknown, uncooperative and spinning target for spacecraft proximity operations," Ph.D. thesis, Massachusetts Institute of Technology, Department of Aeronautics and Astronautics, 2013.

[14] Setterfield, T. P., Miller, D. W., Leonard, J. J., and Saenz-Otero, A., "Mapping and determining the center of mass of a rotating object using a moving observer," *The International Journal of Robotics Research*, Vol. 37, No. 1, 2018, pp. 83–103.

[15] Dor, M., Driver, T., Getzandanner, K., and Tsiotras, P., "AstroSLAM: Autonomous monocular navigation in the vicinity of a celestial small body—Theory and experiments," *The International Journal of Robotics Research*, Vol. 43, No. 11, 2024, pp. 1770–1808.

[16] Florez, J.-D., Dor, M., and Tsiotras, P., "Initialization of Monocular Visual Navigation for Autonomous Agents Using Modified Structure from Small Motion," *2025 American Control Conference (ACC)*, 2025, pp. 5184–5189.

[17] Bi, W., Meng, Y., Wang, Y., Liu, Y., Yin, H., Wu, H., and Liu, H., "Failure mechanisms of a silicon-based CMOS image sensor irradiated by a 1550 nm nanosecond laser," *Opt. Express*, Vol. 32, No. 3, 2024, pp. 4709–4719.

[18] Ruel, S., Luu, T., and Berube, A., "Space shuttle testing of the TriDAR 3D rendezvous and docking sensor," *Journal of Field Robotics*, Vol. 29, No. 4, 2012, pp. 535–553.

[19] Cavrois, B., Vergnol, A., Donnard, A., Casiez, P., and Mongrard, O., "LIRIS demonstrator on ATV5: a step beyond for European non cooperative navigation system," *AIAA Guidance, Navigation, and Control Conference*, 2015.

[20] Civardi, G. L., Piccinin, M., Lavagna, M., et al., "Small bodies IR imaging for vision based relative navigation and mapping enhancement," *7th IAA Planetary Defense Conference (PDC 2021)*, 2021.

[21] McBryde, C. R., "Spacecraft Visual Navigation Using Appearance Matching and Multi-Spectral Sensor Fusion," Ph.D. thesis, Georgia Institute of Technology, Atlanta, GA, May 2018. Doctor of Philosophy with a Major in Aerospace Engineering.

[22] Civardi, G. L., Bechini, M., Quirino, M., Colombo, A., Piccinin, M., and Lavagna, M., "Generation of fused visible and thermal-infrared images for uncooperative spacecraft proximity navigation," *Advances in Space Research*, Vol. 73, No. 11, 2024, pp. 5501–5520. Recent Advances in Satellite Constellations and Formation Flying.

[23] Civardi, G. L., Bussolino, M., Quirino, M., Bechini, M., Lavagna, M., et al., "Uncooperative Spacecraft Relative Navigation via Visible and Thermal-Infrared Image Fusion," *75th International Astronautical Congress (IAC 2024)*, 2024.

[24] Clohessy, W. H., and Wiltshire, R. S., "Terminal Guidance System for Satellite Rendezvous," *Journal of the Aerospace Sciences*, Vol. 27, No. 9, 1960, pp. 653–658. Publisher: American Institute of Aeronautics and Astronautics.

[25] Schaub, H., and Junkins, J. L., *Analytical Mechanics of Space Systems*, fourth edition. ed., AIAA education series, American Institute of Aeronautics and Astronautics, Inc., Reston, VA, 2018.

[26] Gilmore, D. G., *Spacecraft Thermal Control Handbook, Volume 1 - Fundamental Technologies (2nd Edition)*, American Institute of Aeronautics and Astronautics/Aerospace Press (AIAA), 2002.

[27] Rosinol, A., Abate, M., Chang, Y., and Carlone, L., "Kimera: an open-source library for real-time metric-semantic localization and mapping," *2020 IEEE International Conference on Robotics and Automation (ICRA)*, IEEE, 2020, pp. 1689–1696.

[28] Abate, M., Chang, Y., Hughes, N., and Carlone, L., "Kimera2: Robust and Accurate Metric-Semantic SLAM in the Real World," *Experimental Robotics*, edited by M. H. Ang Jr and O. Khatib, Springer Nature Switzerland, Cham, 2024, pp. 81–95.

[29] Bavirisetti, D. P., and Dhuli, R., "Fusion of Infrared and Visible Sensor Images Based on Anisotropic Diffusion and Karhunen-Loeve Transform," *IEEE Sensors Journal*, Vol. 16, No. 1, 2016, pp. 203–209.

[30] Bavirisetti, D. P., and Dhuli, R., "Two-scale image fusion of visible and infrared images using saliency detection," *Infrared Physics & Technology*, Vol. 76, 2016, pp. 52–64.

[31] Perona, P., and Malik, J., "Scale-space and edge detection using anisotropic diffusion," *IEEE Transactions on Pattern Analysis and Machine Intelligence*, Vol. 12, No. 7, 1990, pp. 629–639.

[32] Hotelling, H., "Analysis of a complex of statistical variables into principal components." *Journal of Educational Psychology*, Vol. 24, No. 6, 1933, p. 417.

[33] Karhunen, K., "Über lineare Methoden in der Wahrscheinlichkeitsrechnung," *Ann. Acad. Sci. Fennicae*, Vol. 37, 1947, p. 1.

[34] Loeve, M., "Fonctions aléatoires du second ordre," *Processus stochastique et mouvement Brownien*, 1948, pp. 366–420.

[35] Fiengo, A., Bravo, J. I., Rosa, P., Guercio, N., Christy, J., and Dubanchet, V., "Multispectral Sensing for Relative Navigation," *Proceedings of the 8th European Conference for Aeronautics and Space Sciences (EUCASS)*, 2019.

[36] Barral, H., Arias, P., and Davy, A., "Fixed Pattern Noise Removal for Multi-View Single-Sensor Infrared Camera," *Proceedings of the IEEE/CVF Winter Conference on Applications of Computer Vision (WACV)*, 2024, pp. 1669–1678.

[37] Vallado, D., Crawford, P., Hujsak, R., and Kelso, T., "Revisiting Spacetrack Report #3," *AIAA/AAS Astrodynamics Specialist Conference and Exhibit*, 2006.

[38] Zuiderveld, K., *Contrast limited adaptive histogram equalization*, Academic Press Professional, Inc., USA, 1994, p. 474–485.

[39] Grupp, M., "evo: Python package for the evaluation of odometry and SLAM." `https://github.com/MichaelGrupp/evo`, 2017.

[40] Qin, L., Wu, C., Kong, X., You, Y., and Zhao, Z., "BVT-SLAM: A Binocular Visible-Thermal Sensors SLAM System in Low-Light Environments," *IEEE Sensors Journal*, Vol. 24, No. 7, 2024, pp. 11599–11609.